

## Chapter 5

# Summary and dynamic modeling of earthquakes sequences on the Longitudinal Valley Fault: implications for friction properties

### 5.1 Introduction

The kinematic analysis performed over the 1997-2011 period (chapter 2, *Thomas et al.*, to be submitted) suggests that the slip on the Longitudinal Valley Fault (LVF) is controlled by a complex patchwork of velocity-weakening (VW) patches where the Chengkung earthquake, the background seismicity and the aftershocks can nucleate, and velocity-strengthening (VS) patches, which produce aseismic creep in the interseismic period or during postseismic transients. The interseismic, coseismic and postseismic models complement each other and, to the first order, this simple picture compares well with theoretical models of earthquakes sequences based on rate-and-state friction laws, where the slip mode on the fault is controlled by the lateral and depth variation of frictional properties (e.g., *Dieterich*, 1979; *Ruina*, 1983; *Dieterich*, 1992, 1994; *Lapusta et al.*, 2000; *Lapusta and Liu*, 2009; *Rice and Ben-Zion*, 1996; *Scholz*, 1998; *Kaneko et al.*, 2010; *Barbot et al.*, 2012).

In this last chapter, we propose to analyse further the results from the kinematic inversion of geodetic and seismological data on the LVF (chapter 2, *Thomas et al.*, to be submitted), to evaluate the fault friction properties and to develop a realistic 3D dynamic model of the seismic “cycle” on the southern section of the LVF.

### 5.2 Slip history on the LVF over the 2003 earthquake area

In chapter 2, we were able to determine the time evolution of slip on the LVF over the period 1997-2011, encompassing the 2003 Chengkung earthquake and the pre- and postseismic period. We

now focus on the southern section, around the Chengkung earthquake rupture area, which is best constrained and displays the most noticeable temporal and spatial variations of slip.

The results discussed in chapter 2 are summarized in Figure 5.1, which provides a synthetic view of the time evolution of fault slip in the Chengkung earthquake area over the study period. The map view displays the coupling model (see Figure 2.10a for location), and the time evolution of slip at 6 representative patches is plotted on the right side of figure 5.1 (see section 2.7 in chapter 2 for a description of the time series). The cumulative slip vector at each epoch is projected onto the direction of the long-term slip vector, predicted by the block motion of the Coastal Range relative to the Central Range. As discussed in chapter 2, the spatial resolution of the inversion is typically of the order of less than 1 km near the surface. It increases to about 5 km beneath the coastline, where the fault depth is about 20 km, and it increases gradually to about 15 km at the downdip extent of the model, at the depth of  $\sim 30$  km.

Along-dip variations of slip through time, for three vertical sections on the LVF, are displayed on the left side of Figure 5.1 (see map view for location). For each graph, we average the slip along strike determined at all the patches at the same depth, within a swath spanning three to four patches. Then we plot the cumulative slip along dip with an increment of one year for the preseismic and postseismic periods. The last preseismic curve was chosen to represent the total slip accumulated right before the Chenkung earthquake, and the first postseismic curve represents the cumulative slip one year after the main event. Therefore, the areas in red represent the slip due to the coseismic event only. North of the locked patch, section A1 averages over 3 patches along strike. Section A2 is a four-patches-wide swath, centered right on the zone of maximum coseismic slip. Section A3 averages the cumulative slip over 3 patches and it is located south of the locked zone.

#### *Northern section A1*

The northern section A1 displays mostly creep before and after the main event, at shallow depth (less than 5km) as well as on the deep (more than 20 km) portion of the fault, but also records coseismic slip ( $\sim 25$  cm at the maximum). Near the surface, the average creep rate is estimated to be around 5 cm/yr before the event. It increases abruptly at the time of the Chengkung earthquake and decreases gradually during the postseismic period. In contrast, the Chengkung earthquake seems to have only slightly enhanced the creep rate on the deeper section of the fault (more than 18 km), and postseismic relaxation is hardly visible over the 7-year postseismic period. At the intermediate depths (between about 7 km and 18 km) section A1 shows that the fault was partially locked, with a creep rate about half the long term slip rate, before and after the Chengkung earthquake.

#### *Middle section A2*

Section A2 spans the area with the highest coupling and corresponds to the area where most of

the coseismic slip occurs. Before December 2003, this section of the fault behaves in a fashion very similar to A1, though with a slower creep rate ( $\sim 4$  cm/yr at shallow depth and for the deep creeping part). In the 8 - 15 km depth range, the fault was  $\sim 80\%$  locked in the preseismic period and relocks nearly immediately after the Chengkung Earthquake. The rupture area of the 2003 earthquake coincides approximately with the area which was locked in the preseismic period, although somewhat offset to larger depths. In contrast, the rupture hardly reaches the surface. Coseismic slip reaches a maximum of  $\sim 0.8$  m at 18 km depth. As we illustrated in Figure 2.20 (chapter 2), the overlap at depth could be partially due to the smoothing induced by the regularization of our inversions, but not entirely. After the Chengkung earthquake, aseismic slip occurs at shallow depth, with a creep rate  $\sim 2$  times higher than during the preseismic period, and it relaxes to nearly its pre-seismic value within a year. Some increase of creep rate is also inferred at depth, but no clear relaxation is observed over the 7 years following the main event.

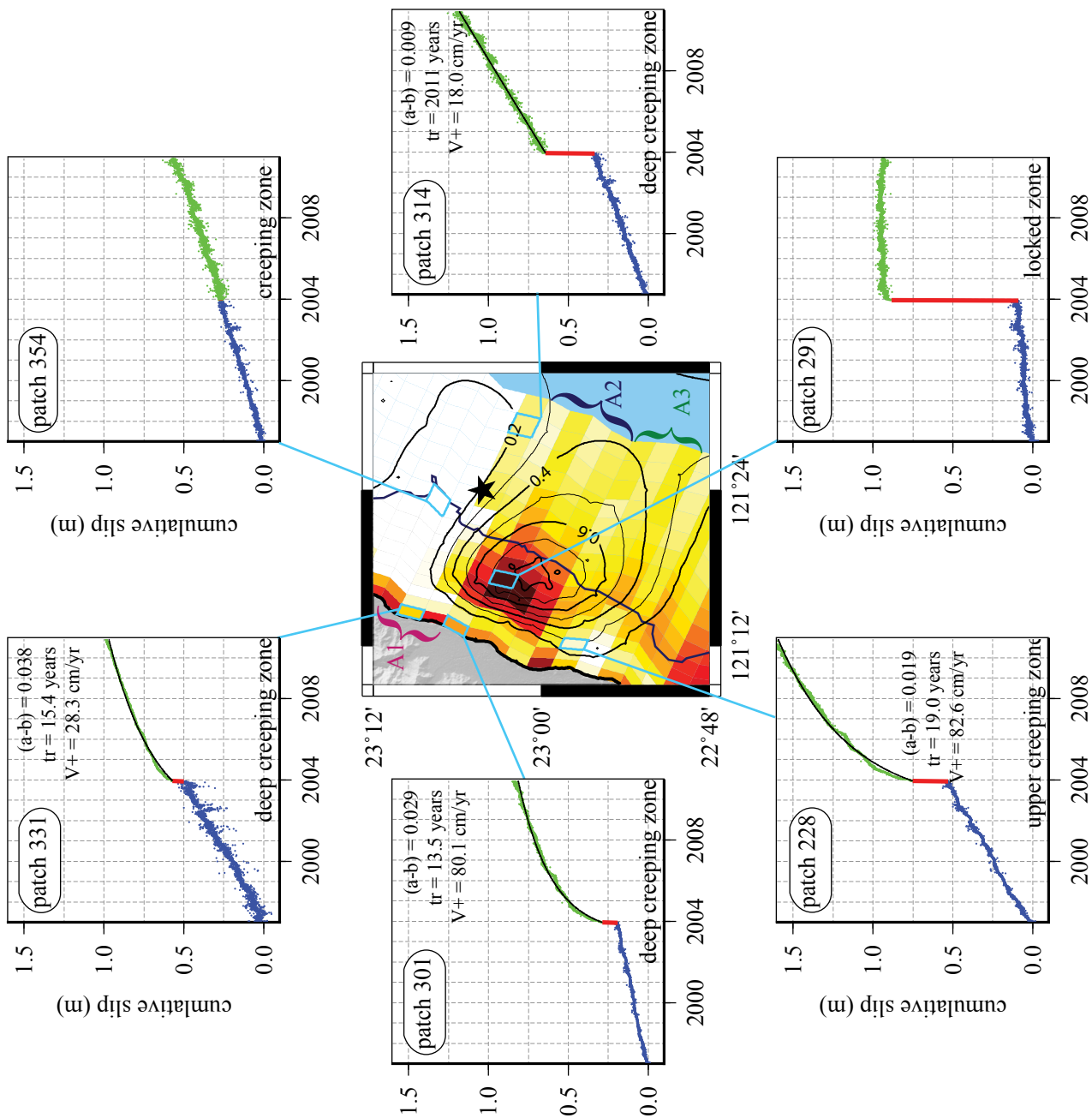
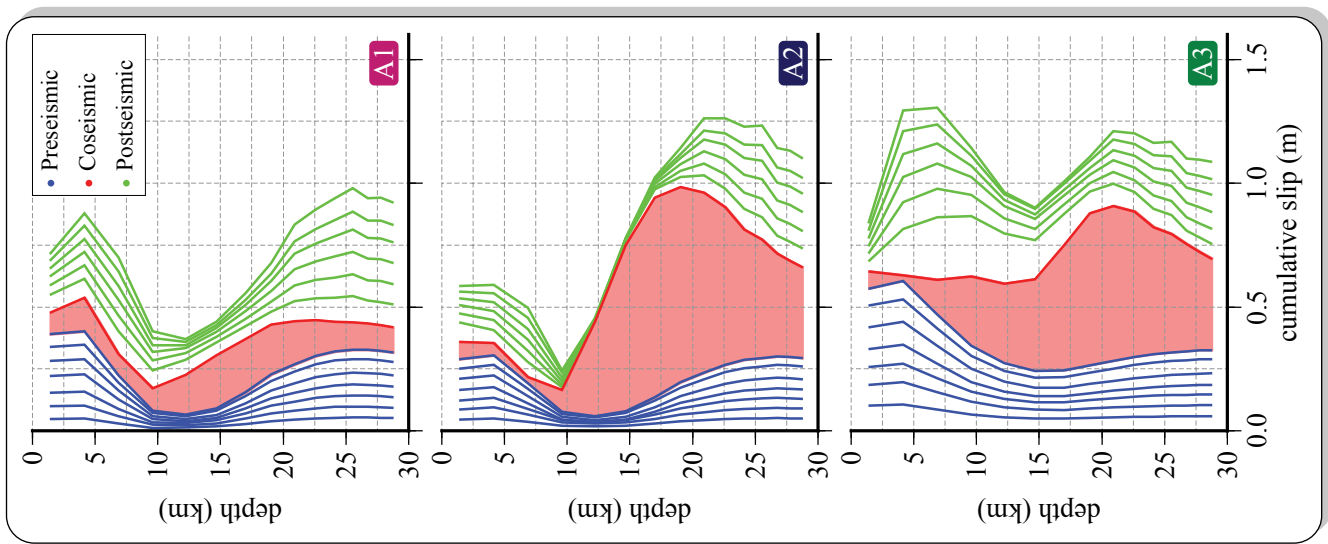
### *Southern section A3*

Section A3 shows a large creep rate at shallow depth (less than 5 km) both before and after the 2003 earthquake, of about 8 cm/yr. At greater depth, the fault is also creeping throughout the study period, though at a lower rate of about 4.5 cm/yr. During the Chengkung earthquake, this section of the LVF seems to have produced some slip with a maximum of  $\sim 0.6$  m at 20 km depth and no significant coseismic slip in the 0-5 km depth range. High postseismic slip is observed at shallow depth (3-12 km) during the first few years following the main shock, with a maximum rate of 23.5 cm/yr around 7.5 km, but the creep rate rapidly slows down to interseismic values. Some afterslip is inferred in the first year at intermediate depths (from 12 to 22 km), but the fault apparently locks up later on. The deepest portion of the fault (from 22 km to 30 km) displays constant slip rate, with a value slightly higher than before the 2003 earthquake.

Altogether, the kinematic model shows that this portion of the fault has been mostly creeping over the study period, with the Chengkung earthquake and aftershocks accounting for only about 20% of the released moment (or equivalent slip potency) (chapter 2). Creep is, however, non-uniform, with a clear deficit of creep in a  $10 \text{ km} \times 12 \text{ km}$  partially locked zone. The Chengkung earthquake  $12 \text{ km} \times 16 \text{ km}$  rupture area approximately coincides with the locked fault zone, although it is broader and offset the deeper portion of the fault. The overlap between the creeping zone and the rupture area could partly be due to the smearing induced by the spatial resolution of our inversions. Hence, to the first order, it seems that it would be appropriate to represent this fault segment as essentially one VW patch embedded in a creeping zone displaying VS friction. Over the 15 years of the study period, coseismic and aseismic slip do not quite even out to uniform slip. In fact, the cumulative slip is, on average, larger than the 0.7 m that would have occurred if the fault had been

creeping at its long term slip rate of about 4.5 cm/yr. This is consistent with the finding that the return period of  $M_w$  6.5 earthquakes, similar to the Chengkung earthquake, needs to be of the order of 36 years, so that the moment released by afterslip and coseismic slip adds up to compensate the deficit of the moment accumulating during the interseismic period (chapter 2). The kinematic model does, however, suggest a somewhat more complicated seismic cycle pattern than the repetition of Chengkung-like earthquakes. In particular, it looks like the coseismic slip and afterslip do not compensate for the deficit of slip on the upper part of the locked fault zone, along sections A1 and A2. Presumably, recurring earthquakes must have different but complementary slip distributions to even out the heterogeneities of slip recorded for a single event. In spite of this complexity, the kinematic model is relatively simple and compares well enough with the idealized seismic cycle models presented next, so that a quantitative comparison with prediction from dynamic modeling simulations is possible.

Figure 5.1: Slip on the fault through time from inversions of pre- and postseismic period and coseismic slip due to the Chengkung earthquake (chapter 2). (See next Page). The map view shows a close-up view of the coupling model on the LVF (see Figure 2.10a for location), with the contour lines of the coseismic slip model (black lines) and epicenter (star) of the 2003 Chengkung earthquake. Graphs around the map view show the time evolution of slip at 6 patches along the direction of the slip vector predicted by the block motion of the Coastal Range relative to the Central Range. Blue, red and green curves represent, respectively, the pre-, co- and postseismic periods. Patches 331, 301, and 228 sample the upper creeping zone. Patch 291 is characteristic of the zone which was locked before the Chengkung earthquake, slipped during the event, and relocked immediately after. Patches 314 and 354 illustrate the behavior of the deeper fault portion which is most poorly resolved. Black curves correspond to the fit of the retrieved patch time series, following the relaxation law as described in *Perfettini et al.* (2010) (equation 5.1). The three panels on the left display the average cumulative slip (in meters) along the three vertical swath sections A1, A2 and A3 located in the map view. Isochrons of cumulative slip are plotted with an increment of one year for the preseismic (blue) and the postseismic (green) periods, whereas red shading shows coseismic slip due to the 2003 earthquake.



### 5.3 Prediction of friction parameters from velocity-strengthening friction law

The kinematic analysis displays a spatio-temporal evolution of fault slip qualitatively consistent with seismic cycle models (*Rice, 1993; Lapusta et al., 2000*) based on laboratory-derived rate-and-state laws (*Dieterich, 1979; Ruina, 1983; Dieterich, 1992, 1994, and references therein*). Here, we estimate the frictional parameters that would allow for predicting quantitatively the observed postseismic relaxation. We assume that the fault obeys a rate-and-state friction law (for details see section 4.2.2 in chapter 4).

We compare the time evolution of slip deduced from the inversions of the geodetic data with that predicted from a velocity-strengthening friction law. We assume steady state, since the slip-at-depth time functions retrieved from the inversions do not sample the transient early increase of postseismic slip rate, which would reflect the adjustment of the state variable (*Perfettini and Avouac, 2007; Perfettini and Ampuero, 2008; Fukuda et al., 2009*). The analysis of this short-lived transient would probably require better temporal resolution than the daily resolution of the kinematic model obtained in chapter 2. In the steady-state approximation, for a VS material, the friction law only depends on the slip velocity, and the frictional stress  $\tau$  increases linearly with the logarithm of the sliding velocity  $\dot{U}$ . If elastic interactions among the various creeping patches are ignored an analytical solution can be derived (*Perfettini and Avouac, 2004*), which can then be used to infer the fault friction properties, as it has been done in a number of studies (*e.g., Perfettini et al., 2010; Hsu et al., 2006*). This model predicts that postseismic slip  $U(t)$  evolves as:

$$U(t) \approx V_{pl} t_r \log \left[ 1 + \frac{V^+}{V_{pl} t_r} t \right], \quad (5.1)$$

where  $t_r$  is the relaxation time,  $V_{pl}$  the long-term slip rate, and  $V^+$  is the sliding velocity on the fault immediately after the earthquake. According to this law, the ratio  $\frac{V^+}{V_{pl}}$  depends on the friction parameters ( $a - b$ ), the normal stress  $\bar{\sigma}$ , and the static Coulomb stress change induced by the main shock ( $\Delta CFF$ ) (*Perfettini and Avouac, 2004; Perfettini et al., 2010*), as follows:

$$(a - b) = \frac{\Delta CFF}{\bar{\sigma} \log \left( \frac{V^+}{V_{pl}} \right)}. \quad (5.2)$$

The relaxation time,  $t_r$ , depends on the frictional parameters but also on the stressing rate,  $\dot{\tau}$ , according to:

$$t_r = \frac{(a - b)\sigma}{\dot{\tau}}. \quad (5.3)$$

An estimation of the friction parameters ( $a - b$ ) can therefore be deduced by computing the static Coulomb stress change from our coseismic model (section 2.5 in chapter 2) and fitting the

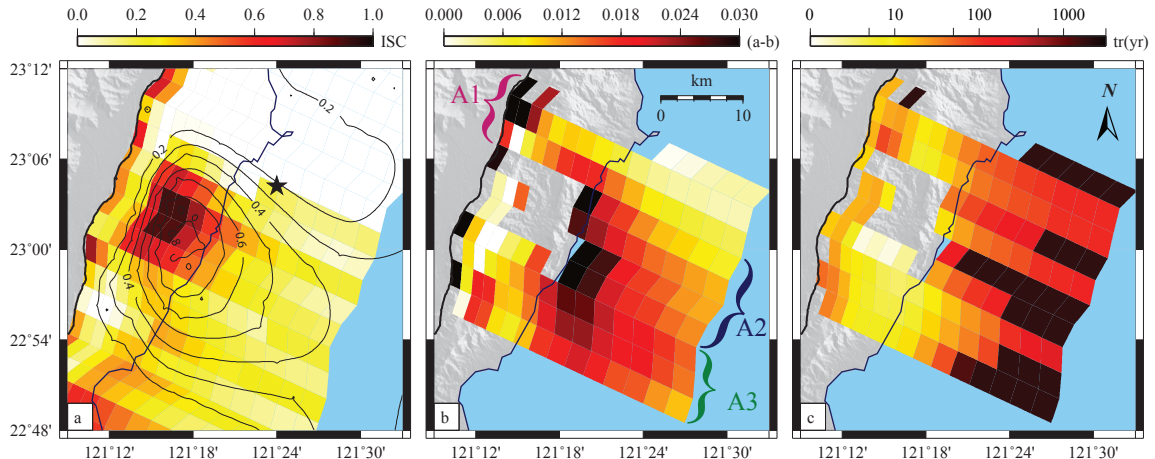


Figure 5.2: (a) The map view shows the coupling model on the LVF for the Chengkung area (see Figure 2.10a for location), with contour lines of the coseismic slip model (black lines) and epicenter (star) of the 2003 Chengkung earthquake. (b) Frictional parameters ( $a - b$ ) and (c) relaxation time  $t_r$  predicted from the velocity-strengthening friction law (equation 5.1). Only patches that show accelerated creep after the Chengkung earthquake were selected.

time evolution of slip for all patches that record postseismic slip (Figure 5.1 and 5.2). This calculation can be done based on the semi-analytical solution of *Okada* (1992). The values for upper patches should, however, be taken with caution, since  $(a - b)$  grows toward infinity for small values of  $\bar{\sigma}$ .

The frictional parameter  $(a - b)$ , calculated assuming the hydrostatic pore pressure and rock density of  $2800 \text{ kg/m}^3$ , varies with depth from near velocity-neutral to 0.03. This is comparable to the values obtained in laboratory experiments for illite-rich lithology, similar in lithology to the Lichi Mélange, and assumed to be representative of subduction mélanges in general (*den Hartog et al.*, 2012a; *Ikari et al.*, 2011a) (Figures 5.3, 5.2 and 5.4a). If we plot those values against the temperature derived from the thermokinematic model of *Simoës et al.* (2007a) (Figure 5.3), we observe a trend similar to that observed experimentally on illite-rich gouges (*den Hartog et al.*, 2012a) (Figure 5.4a), for panels A3 and A2. The values of  $(a - b)$  derived for patches in section A1 are not as well constrained, since almost no postseismic relaxation occurs on that section of the fault (see section 5.2 and Figure 5.1). Therefore, the rate-dependency of friction derived from our kinematic model (Figure 5.3) seems comparable to the values measured in the lab for a clay-rich fault zone lithology (Figure 5.4). In addition, we observe that patches, inferred to be VW patches, fall into the  $250 - 400^\circ\text{C}$  range for which a VW behavior is observed in the laboratory. So the temperature may well be the factor explaining along-dip variations of frictional properties: from VS at  $150 - 250^\circ\text{C}$  to VW at  $250 - 375^\circ\text{C}$ , and VS again for temperatures higher than  $380^\circ\text{C}$ . This temperature dependency of illite-fault gouges could be applied to the section A2 in particular, but fails to explain the observed lateral variations, since the temperature is probably quite uniform along strike on the LVF. This discussion shows that some of our results are quite consistent with results

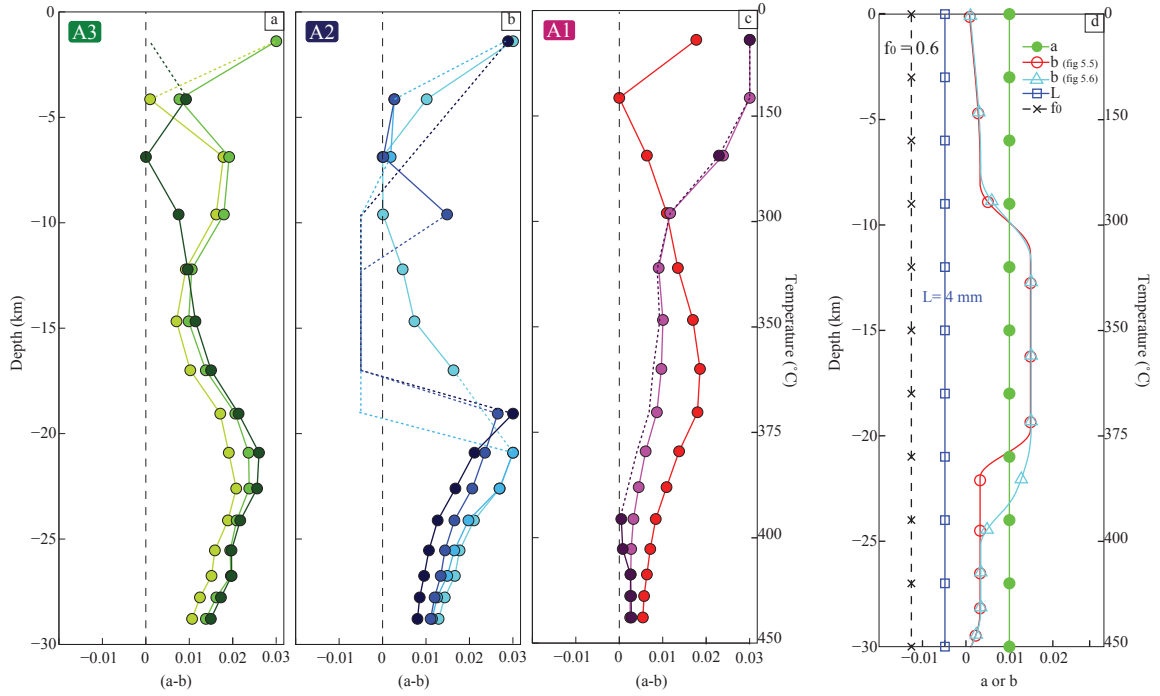


Figure 5.3: (a), (b) and (c): along-dip variations of frictional parameters ( $a - b$ ) predicted from a velocity-strengthening friction law (equation 5.1) for patches within swath sections A1, A2 and A3, respectively (see Figure 5.2 for location). Dashed lines show hypothetical interpolated values of ( $a - b$ ) based on the coupling model (Figure 5.2a), *i.e.*, if the patch is locked ( $ISC > 0.8$ ) we assume that the friction law is velocity-weakening, and if the patch was creeping before the Chenkung earthquake, we interpolate with the nearby values. The temperature on the LVF is retrieved from *Simoes et al. (2007a)*. (d) Down-dip variations of  $a$ ,  $b$ ,  $L$  and  $f_0$  vs temperature and depth assumed in the dynamic simulations (Figures 5.5 and 5.6) for the fault portion that models segment A2.

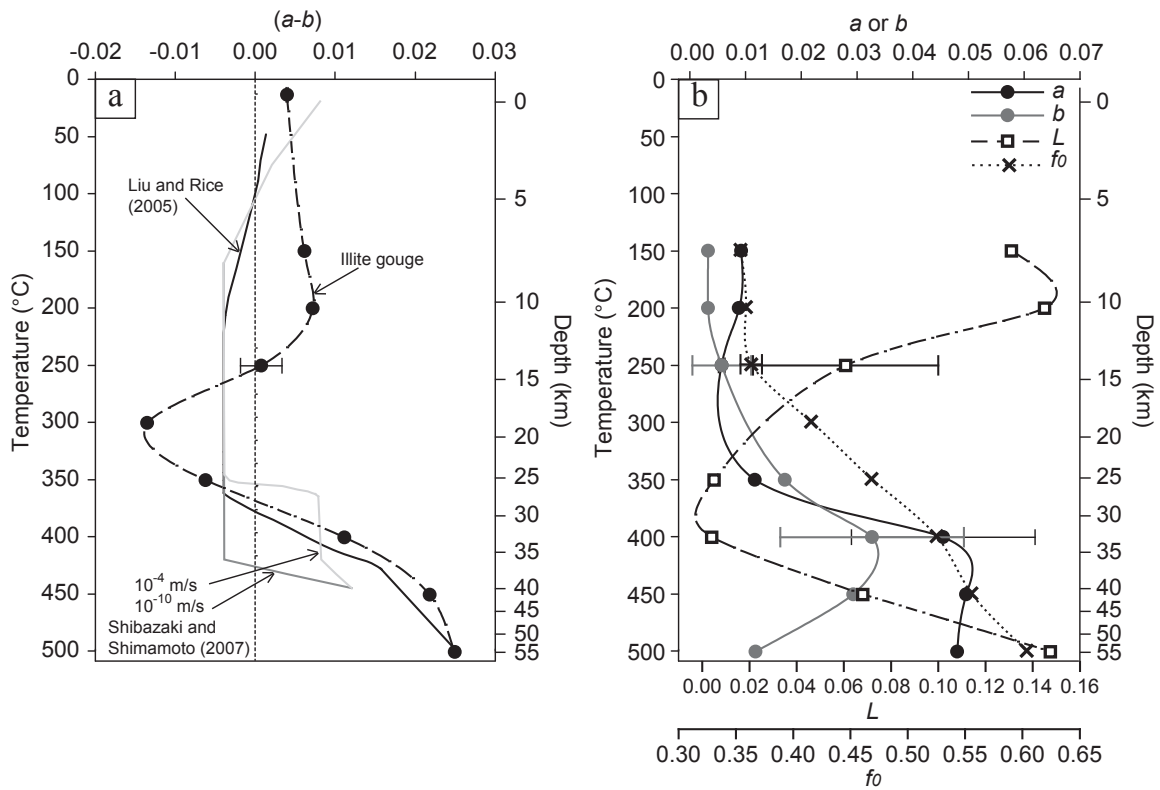


Figure 5.4: Figure from *den Hartog et al. (2012a)* (slight modification). (a) The values of  $(a - b)$  for illite-rich gouge derived from the laboratory measurements in *den Hartog et al. (2012b)*, shown as dots. The error bars represent plus or minus one standard deviation. The dashed trend line emphasizes the data trend for clarity. The pressure-temperature path for Shikoku of *Peacock (2009)* is used. For comparison, the profile of *Liu and Rice (2005)* for the example of the Shikoku subduction zone plus two profiles of *Shibazaki and Shimamoto (2007)* are given, for different sliding velocities. The profiles given in the two respective studies are based in part on the data for wet granite (*Blanpied et al., 1998*) and dry halite (*Shimamoto, 1986*), respectively. (b) Profiles of  $a$ ,  $b$ ,  $L$ , and  $f_0$  vs temperature. Values of  $a$ ,  $b$ , and  $L$  (in mm) are derived from velocity steps from 1 to 10 mm/s. Error bars represent plus or minus one standard deviation.

from experimental laboratory studies. We should, however, forewarn that the thermokinematic model is not well-constrained for the LVF, given the lack of thermometric and thermochronological data from the Coastal Range. Consequently, those observations should be taken with caution. An alternative possible explanation for the presence of VW patches inside a VS matrix can also be related to the presence of competent blocks (*Fagereng and Sibson, 2010*), which we know can be of kilometric size in the Lichi Mélange (see section 3.2.3).

Finally, the  $(a - b)$  values obtained at shallow depth ( $\sim 5$  km) from our inversion compare well with the estimated values of 0.013 before the Chengkung EQ and 0.0066 after the main event, derived from the modeling of seasonal variations of slip rate induced by pore-fluid pressure variations *Chang et al. (2009)*.

## 5.4 Dynamic modeling of earthquake sequences

The analysis based on the analytical formula described above (equation 5.1 and 5.2) (*Perfettini and Avouac, 2004; Perfettini et al., 2010*), derived from the equation of motion of a one-degree-of-freedom spring-and-slider system, may be too simplistic, in particular because it ignores the interactions between neighboring patches due to elastic stress transfer. In addition, this analysis does not provide any insight on the frictional properties of the VW patches or on the reference friction coefficient  $f_0$ . To improve our understanding of the factors that govern the slip behavior of the LVF, we therefore carry out numerical fully-dynamic (FD) simulations of earthquake sequences and slow slip to qualitatively reproduce the wide range of observations for the southern segment of the LVF.

The model set up is designed based on the kinematic model summarized in Figure 5.1 (Chapter 2, *Thomas et al.*, to be submitted). We follow an approach similar to that of *Barbot et al. (2012)* who developed a model calibrated to reproduce the seismic cycle on the Parkfield segment of the San Andreas fault. As discussed in chapter 4, a quasi-dynamic approximation would be less costly but the inferences made could be biased. We therefore conduct only FD simulations.

The model assumes a thrust fault segment embedded into an uniform, isotropic, elastic medium, loaded at the average long-term slip rate on the fault (4.5 cm/yr) and governed by the rate-and-state friction law. A patch with the VW friction ( $a - b = -0.005$ ), where seismic slip can nucleate, is embedded in a VS area for which we apply the value ( $a - b = 0.0066$ ) determined by (*Chang et al., 2009*) (Figures 5.3d, 5.5a and 5.6a). To account for the listric shape of the fault, we define the normal stress as if we were along-dip on the LVF (Figures 5.5b and 5.6b). Hereafter, to facilitate the comparison with the kinematic inversion of fault slip, we plot the equivalent depth (computed from the formula  $\rho g z$ ) rather than the “true” depth of our model. In our simulations, the characteristic slip distance  $L = 4$  mm, the Poisson ratio  $\nu = 0.25$ , and the reference friction coefficient  $f_0 = 0.6$

are constant over the fault (Figure 5.3d). The pre-stress  $\tau_0$  is uniform on the fault, except for one location where  $\tau_0$  is slightly increased over a  $1 \times 1 \text{ km}^2$  patch, at the right-bottom boundary between the VS and VW regions. This set-up promotes the nucleation of the first event. More details about the elastodynamic relations and the constitutive laws of those models can be found in chapter 4 (section 4.2) and in *Lapusta and Liu (2009)*.

The frictional parameters within the VW zone are adjusted so that ruptures of the whole patch would produce  $M_w$  6.8 earthquakes with a return period comparable to our estimate of 36 years. Because of the computational cost of the FD simulations, we assume a relatively large value of the critical slip-weakening distance  $L$  of 4 mm. This choice yields a nucleation size  $h^*$  of about 1.5 km. We develop two models: one with a sharp boundary between the VW patch and the surrounding VS area, and the other with a more smooth transition down-dip to allow propagation of seismic slip into the deeper VS zone (Figure 5.3d). Results are presented in Figures 5.5 and 5.6, respectively.

The models predict a relatively simple seismic cycle with the quasi-periodic return of similar earthquakes, rupturing the whole VW patch. The relatively large value of the nucleation size, compared to the size of the VW patch, prevents generating smaller size earthquakes. As a result, the model does not produce much complexity. Nevertheless, these simple models succeed in reproducing some key aspects of the seismic cycle on the LVF. First, they both yield seismic events with a magnitude close in  $M_w$  to that of the Chengkung earthquake, although slightly smaller: 6.4 on average for the abrupt transition (Figure 5.5c), and 6.5 for the model with enhanced down-dip seismic slip (Figure 5.6c). The recurrence time of those events are 35.4 and 36.2 years, respectively, consistent with our estimate of the return period of Chengkung-type earthquake on the LVF, *i.e.*, 36 years.

In both models, the seismic ruptures do not reach the surface (Figures 5.5e and 5.6e), indicating that the VS friction on the shallow patch is strong enough, given its down-dip extent, to arrest up-dip propagation of seismic ruptures, as it happened during the Chengkung earthquake. The model with the smooth transition of  $(a - b)$  parameters allows for the ruptures to propagate further down-dip (Figure 5.6e), leading to a slightly larger  $M_W$ . This model is therefore closer to reproducing the down-dip extent of the Chengkung earthquake (Figure 5.1).

Afterslip in the models is equivalent to about half of the coseismic moment, which is a smaller ratio than for the Chengkung earthquake, and the creep rate is back to the interseismic velocity after 5 years, as observed on the LVF at shallow depth, but not on the deep creeping section. These remarks suggest that a better fit would be obtained with a lower value of  $(a - b)$  beneath the VW patch. This would allow the rupture to extend deeper and hence to yield a larger magnitude. Another option to increase the magnitude of the earthquakes rupturing the whole VW patch would be to increase  $b$  within the VW patch, but coherently decrease the parameters  $L$  to hold to the estimated 36 years recurrence time (See *Barbot et al. (2012)* for discussion). Also, a lower value of  $L$  would yield more

complexity and more diversity of the slip distributions.

## 5.5 Conclusion

The spatio-temporel evolution of fault slip on the LVF over the 1997-2011 period is consistent, to the first order, with predictions from a simple model in which a VW patch is embedded in a VS area. We show that the time evolution and spatial distribution of afterslip can be quantitatively explained based on such a model and used to estimate the velocity-dependency of friction at steady-state ( $a - b$ ). We obtain values relatively consistent with the laboratory measurements on clay-rich fault zone gouges comparable to the Lichi Mélange, which borders the southern segment of the LVF. The  $a - b$  parameter varies along-dip, possibly as result of temperature as the laboratory results suggest, but it also varies along-strike, probably for some reason other than temperature variations. A more realistic model of the seismic cycle on the LVF would require adding complexity to the model set-up, for example, by assuming more heterogeneous frictional properties and reducing the nucleation size to get a wider range of earthquake magnitudes. Hence, although the models shown here are relatively satisfying given their simplicity, the model geometry and parameters could certainly be further improved to better quantitatively reproduce the wide range of observations available from the LVF. Note also that another modeling technique than the Boundary Integral Method would be more appropriate to take into account the effect of the free surface (this effect can be correctly taken into account with the Boundary Integral Method only for a vertical fault in mode II) and nonplanar geometry.

Finally, it should be underlined that there is no firm evidence that strong weakening mechanisms, such as thermal pressurization (*Rice, 2006*), occurred during the Chengkung earthquake. However, enhanced seismic weakening could explain that the rupture was able to propagate down-dip beyond the locked VW patch (*e.g. Sibson, 1973; Lachenbruch, 1980; Mase and Smith, 1987; Rudnicki and Chen, 1988; Sleep, 1995; Andrews, 2002; Bizzarri and Cocco, 2006a,b; Rice, 2006; Noda and Lapusta, 2010*). In that case, parameters such as the permeability, friction coefficient, or shear zone width should vary with depth to enhance the thermal pressurization effect in the deeper part but not near the surface.

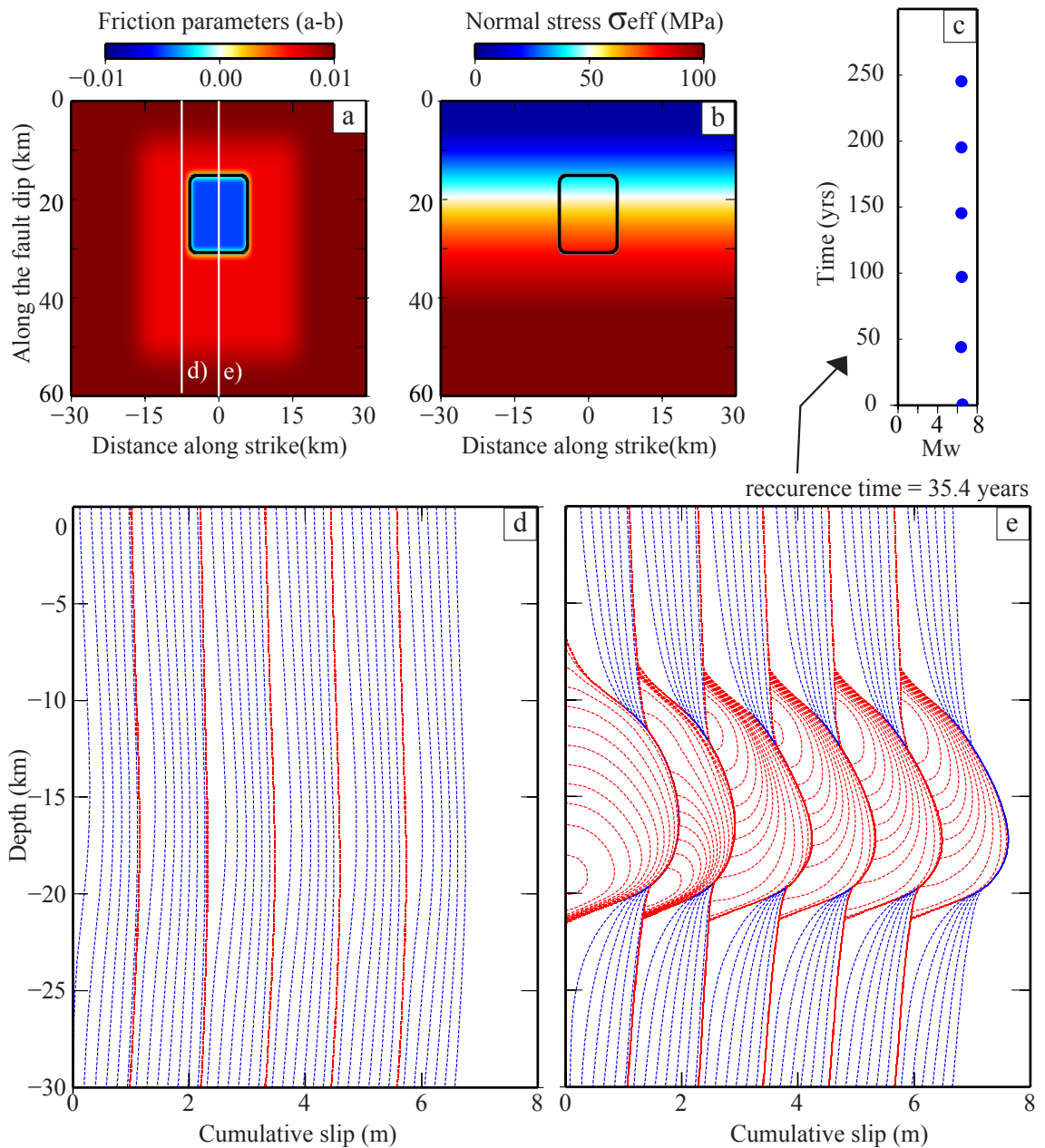


Figure 5.5: 3D simulations of earthquake sequences, with abrupt transition of ( $a - b$ ) parameters at depth. (a) Variation of friction parameters ( $a - b$ ). (b) Along-dip variation of normal stress. (c) Catalogue of simulated seismic events. (d) and (e) Cumulative slip on the fault for two depth profiles, one in the middle of the fault (e) and one on the left side (d). See subfigure (a) for the locations. Red lines are plotted every 2 s when maximum slip velocity exceeds 1 mm/s, while blue lines (every 5 years) illustrate the aseismic behavior of the fault.

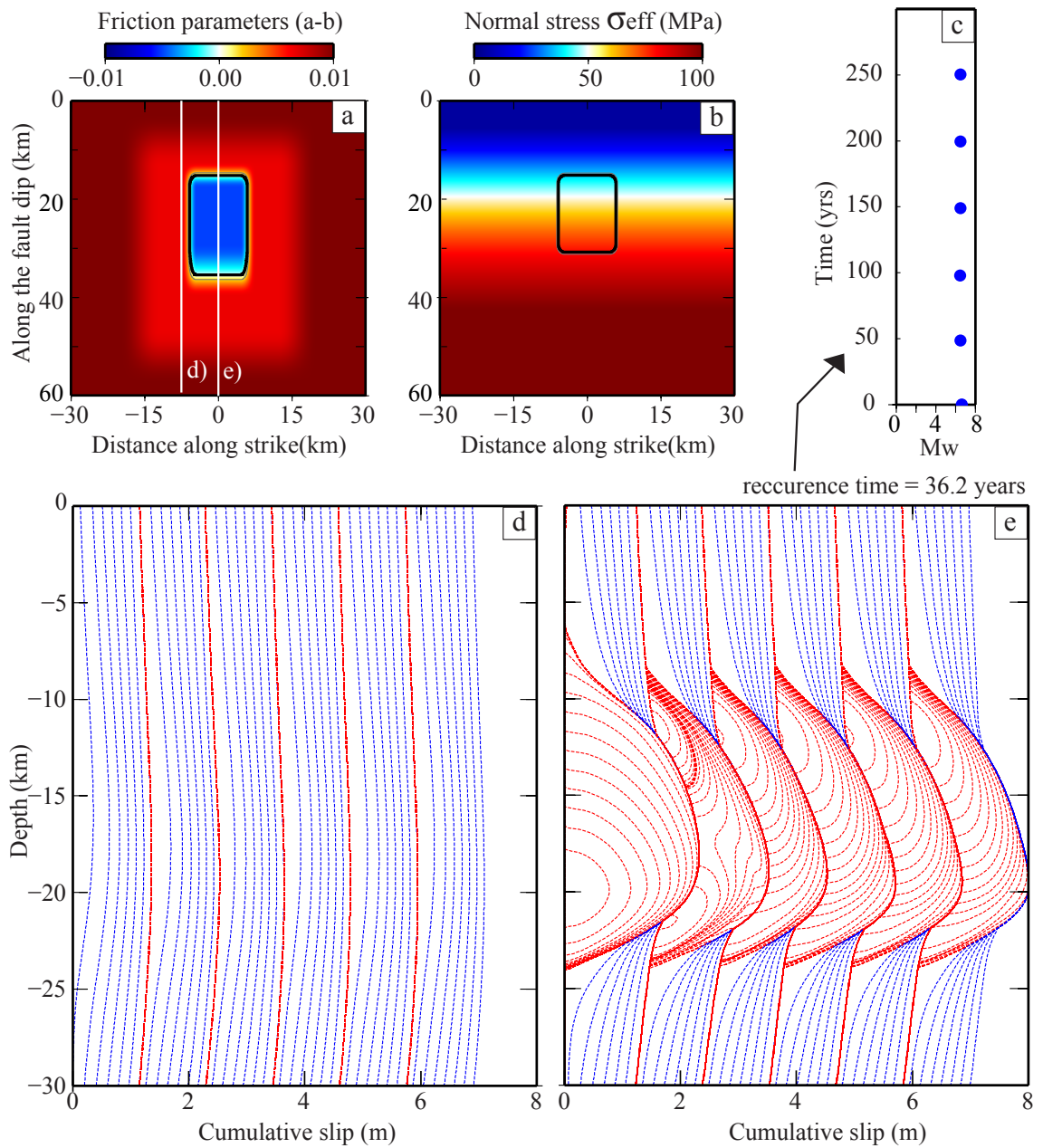


Figure 5.6: 3D simulations of earthquake sequences, with smooth transition of ( $a - b$ ) parameters at depth. (a) Variation of frictional parameters ( $a - b$ ). (b) Along-dip variation of normal stress. (c) Catalogue of simulated seismic events. (d) and (e) Cumulative slip on the fault for two depth profiles, one in the middle of the fault (e) and one on the left side (d). See subfigure (a) for the locations. Red lines are plotted every 2 s when maximum slip velocity exceeds 1 mm/s, while blue lines (every 5 years) illustrate the aseismic behavior of the fault.